J Mater Sci (2018) 53:2911–2927

Metals

Grain boundary phase transformations in PtAu and relevance to thermal stabilization of bulk nanocrystalline metals

C. J. O'Brien[1,*], C. M. Barr[2], P. M. Price[2], K. Hattar[2], and S. M. Foiles[3]

[1] P.O. Box 5800, MS 0748, Albuquerque, NM 87185-0748, USA
[2] P.O. Box 5800, MS 1056, Albuquerque, NM 87185-1056, USA
[3] P.O. Box 5800, MS 1411, Albuquerque, NM 87185-1411, USA

Received: 6 August 2017
Accepted: 10 October 2017
Published online: 31 October 2017

© Springer Science+Business Media, LLC (outside the USA) 2017

ABSTRACT

There has recently been a great deal of interest in employing immiscible solutes to stabilize nanocrystalline microstructures. Existing modeling efforts largely rely on mesoscale Monte Carlo approaches that employ a simplified model of the microstructure and result in highly homogeneous segregation to grain boundaries. However, there is ample evidence from experimental and modeling studies that demonstrates segregation to grain boundaries is highly non-uniform and sensitive to boundary character. This work employs a realistic nanocrystalline microstructure with experimentally relevant global solute concentrations to illustrate inhomogeneous boundary segregation. Experiments quantifying segregation in thin films are reported that corroborate the prediction that grain boundary segregation is highly inhomogeneous. In addition to grain boundary structure modifying the degree of segregation, the existence of a phase transformation between low and high solute content grain boundaries is predicted. In order to conduct this study, new embedded atom method interatomic potentials are developed for Pt, Au, and the PtAu binary alloy.

Introduction

Grain boundaries are a ubiquitous feature of polycrystalline materials that increase in volume fraction as grain size decreases into the nanocrystalline regime. Further, alloy additions are a common, long standing method for tailoring the microstructure and resultant properties of materials. For these reasons, there is a long history of the study of grain boundaries and the interaction of alloy additions and impurities with these interfaces. The current work was motivated by a desire to understand the role of alloying on the stability of nanocrystalline metals. The results presented here, though, have relevance to the thermodynamics of grain boundary alloying at all scales.

Nanocrystalline materials are of great interest due their ability to combine strength and toughness [1],

Address correspondence to E-mail: cjobrie@sandia.gov

DOI 10.1007/s10853-017-1706-1

but often suffer from poor thermal stability of the nanocrystalline grain structure. Much interest has been generated recently in the ability to choose an alloy and composition that can dramatically increase the thermal stability of the microstructure to coarsening as has been observed in a number of alloys such as: W–Ti [2], W–Cr [3], Cu–Ta [4], Fe–Mg, Ni–W [5], Cu–Zr [6], and Fe–Zr [7, 8]. Such alloys are stabilized by either thermodynamic (meta)stability of grains by solute segregation [9, 10], kinetic effects including solute drag and Zener pinning, or a combination of thermodynamic and kinetic mechanisms [11]. Recently, there has been increasing recognition that the topology of the grain boundary structure can dominate thermodynamic stability considerations [12]. Even though thermodynamic stability is likely not the entire reason for the increased thermal stability of particular nanocrystalline alloys, the effect is significant and cannot be discounted.

Current models of the thermodynamic stabilization of nanocrystalline materials [13, 14] rely on Monte Carlo (MC) approaches employing enthalpies of mixing calculated via thermodynamic databases [15]. However, most of the existing MC models assume uniform grain boundary segregation [10, 15] or a simplification of the complexities of the boundary geometry [14, 16]. Such models tend to form a solute-rich phase at the grain boundaries and may even exhibit temperature dependent phase transformations [17]. Antecedents to phase formation on the boundary are found in models of grain boundaries in nanocrystalline materials that suggest a disordered region exists at the grain boundary [18]. The formation of grain boundary phases (called complexions [19]) is a related idea that has been also shown to increase the thermal stability of nanocrystalline materials in alloys such as CuZr [6].

The structure and resulting range of properties of grain boundaries are much more complex than often appreciated, likely due to their characterization with metrics such as coincident site lattice (CSL) Σ value and misorientation. Recent investigations have demonstrated that a given macroscopic planar grain boundary can exist in one of multiple metastable states due to the presence of microscopic structures with nearly degenerate energies [20]. The variability of planar boundary properties is highlighted in recent computational studies [21] that have concentrated on the variability of grain boundary energy [22, 23] and mobility [24] over the 5-dimensional geometric space of grain boundaries.

There has been increasing evidence for and recognition of the substantial variability of grain boundary segregation in a given alloy with the degree of segregation depending on the grain boundary character. Barr and coworkers [25, 26] have observed the variation of radiation induced segregation with grain boundary character. Atom-probe tomography has been employed to examine the variation of local boundary composition at grain boundaries in Nb-doped ceria [27], carbon segregation at grain boundaries in ferrite [28], and tungsten and chromium segregation in a ferritic alloy [29]. Change in grain boundary structure due to segregation has been observed in Fe–Au twist grain boundaries by [30].

The possibility of multiple phases associated with alloy grain boundaries has also been discussed. Wynblatt and Chatain [31] developed a model of phase separation in grain boundaries in analogy with surface miscibility gaps [32]. In addition, abrupt changes in boundary composition with temperature have been observed experimentally [33] and seen in MC models [17]. Phase field models of grain boundaries in multi-component systems [34–36] predict the existence of transitions between solute-poor and solute-rich grain boundary phases possibly associated with transitions between ordered and disordered states of the boundary.

In this work, the PtAu noble metal system is studied as a model system to aid in elucidating the effects of kinetic versus thermodynamic stabilization of nanocrystalline materials. This system was chosen because it has a large miscibility gap consistent with the conditions expected to produce alloy stabilization of grain boundaries and should avoid the formation of second phase and oxide particles which could result in Zener pinning. The latter considerations are particularly important in the choice of this alloy for concurrent experimental work as prior experimental studies have been complicated by the presence of oxides [37]. The Au is a substitutional solute with 4.3% size mismatch (with the current potential) making chemical interaction, rather than strain, the dominant mechanism for segregation. Plus, PtAu alloys are predicted by previous models [15] to stabilize nanocrystalline microstructures, partially due to the immiscibility of the system that encourages solute segregation.

Existing potentials for noble metal alloys such as that of [38, 39], included only minimal alloy data during parameterization. This weakness originates from a lack of data regarding the noble metal intermetallics that makes it difficult to fit in the traditional scheme where specific experimental properties are used to fit embedded atom method (EAM) potentials. Due to the dearth of measured properties for noble metal intermetallics, we instead rely on density functional theory to provide forces and energies of the intermetallics and disordered configurations with which new interatomic potentials for PtAu will be parameterized. This strategy is referred to as force matching [40].

This work focuses on the applying the newly developed potential to generate an equilibrium solute-segregated microstructure. The observation of nonuniform segregation in the microstructure spurred further investigation into what factors may affect such dramatic differences in the degree of segregation. More detailed examinations were made of individual grain boundaries in bicrystals that demonstrated that there exists a phase transition between states with a high and low degree of segregation that occurs for bulk concentrations well within the solid solubility limit of Au in Pt.

Methodology

One of the challenges in atomistic-scale simulations of alloy systems is how to place the atoms and, further, how to assign the chemical species to the atoms. Historically, one approach is to perform MC simulations which include thermal displacements in addition to compositional changes [41–43]. While this approach in principle samples the positional phase space, experience has shown that it does not efficiently find significant structural changes. Two different hybrid schemes were employed in this study to obtain equilibrium atomic distributions. Both of these approaches alternated between molecular dynamics (MD) simulations at temperature to equilibrate the structural aspects and MC simulations to equilibrate the compositional degrees of freedom. The techniques differed in the thermodynamic ensemble of the MC simulations. The MD component in each case was performed by the LAMMPS package [44]. Both approaches were conducted with the embedded atom method potential for PtAu developed for this study (See "Appendix 1" section for details).

Approach (a) proceeded by first randomly populating sites in the boundary to a predetermined concentration. A MC simulation phase was then performed whereby two atoms are selected. If they were different chemical species, their chemical identities were swapped and the energy difference was computed. This swap was retained with a probability based on the Boltzman factor for the energy change and the assumed temperature. Note that this MC process maintained the number of atoms of each species. Thus approach (a) is sampling the equilibrium canonical ensemble with fixed total numbers of each species. This MC phase was followed by a short constant number of atoms, volume, and temperature (NVT) MD simulation at the desired temperature. The cycle of MC and MD simulations was repeated until an equilibrium configuration is reached.

Approach (b) performs the MC simulations in a semi-grand canonical ensemble where the chemical potential difference is fixed and the relative number of each species is allowed to vary [41, 45]. It is initiated by first randomly populating the boundary with the concentration of Au expected for a given chemical potential and thermally equilibrating for 10 ps with NVT MD. After every 25 time steps (or 0.025 ps) the algorithm randomly selects a number of atoms, equal to the initial number of Au atoms, and attempts to swap the species (Pt–Au, or Au–Pt) of each atom individually with the swap success probability governed by the difference in energy adjusted by the difference in chemical potential between the species. The swapping procedure occurred 100000 times attempting to equilibrate the composition, whereupon an additional 50000 cycles were performed over which the composition is averaged. The bulk concentrations are calibrated to the chemical potential difference in separate simulations on bulk lattices.

Note that both approaches (a) and (b) sample the thermal distribution of the two species. However, they do so in different statistical ensembles and as such show different signatures at two phase coexistence. In approach (b), semi-grand canonical ensemble, the composition will ideally change discontinuously as the chemical potential difference changes past the transition point. In approach (a), canonical ensemble, for an arbitrarily large sample it will separate into regions with the two coexisting concentrations. Overall concentrations between the

coexisting concentrations are thermodynamically unstable. It should also be noted that the MC simulation methods employed here are designed to sample equilibrium, but by the non-diffusional nature of the composition changes they do not provide information on the kinetics of the segregation process.

Two types of microstructure will be modeled in this study, a representative nanocrystalline polycrystal as well as select planar boundaries in simple bicrystal geometries. A realistic nanocrystalline microstructure was generated using the technique of [46], that generates initial microstructures via a phase-field approach that are then populated with atoms. The resultant microstructure reproduces properties such as triple-junction angles much better than may be achieved by the Voronoi construction. Figure 1 illustrates the initial microstructure after equilibrating to 775 K. The solute was distributed throughout the sample using method (a) with a global composition of $15\%_{at}$Au. The microstructure is intended to be representative of the temperature, composition and grain-size of the experimental microstructure employed in this study. This microstructure is used to provide representative Au concentrations present in the bulk grains.

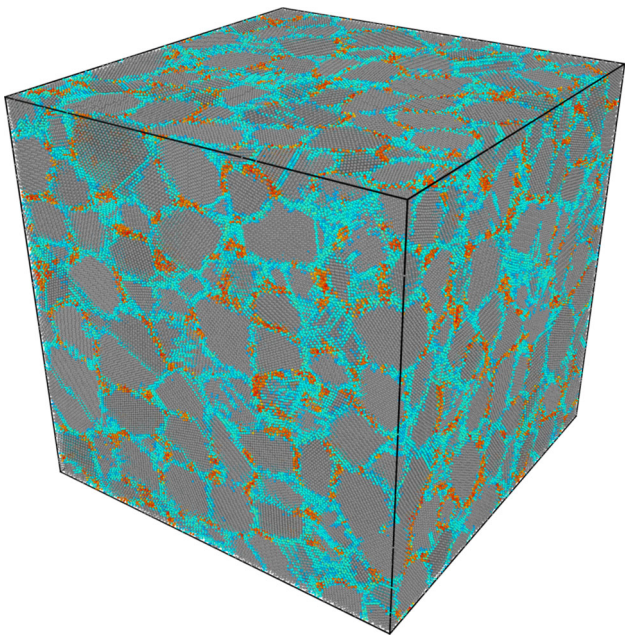

Figure 1 Equilibrium state of a nanocrystalline PtAu alloy with $10\%_{at}$Au overall composition. Atoms are classified by a combination of common neighbor analysis (CNA) [51, 52] and the Centro-symmetry parameter (CSP) [53]. Atoms are colored such that Pt atoms in a local FCC environment are colored gray and Au atoms in a local FCC environment are colored yellow. Pt and Au in a disordered environment (e.g. grain boundaries) are shifted from gray to cyan or yellow to orange, respectively, with increasing disorder as quantified by their CSP.

In order to isolate the segregation behavior of individual grain boundaries, four planar bicrystals are examined. Boundary excess concentration is defined, such that the excess gold concentration is consistent with Cahn's definition [47], as

$$[C^{ex}] = \frac{(N_{Au})_{gb} - (N_{Pt})_{gb}(C_{Au})_{bulk}}{A}, \quad (1)$$

where $(C_{Au})_{bulk}$ is the concentration of Au in the bulk (as the Au:N ratio where N is the total number of Pt and Au atoms), $(N_{Au})_{gb}$ is the number of Au in a region containing $(N)_{gb}$ total atoms in the neighborhood of the grain boundary, and A is the grain boundary area.

To provide experimental support for the model, nominally 40 nm-thick nanocrystalline films were produced by magnetron sputtering Pt-$10\%_{at}$Au onto a polished NaCl substrates. The Pt-$10\%_{at}$Au film was then floated off onto transmission electron microscopy (TEM) Mo mesh grids and annealed in a custom vacuum furnace at 5×10^{-6} Torr and 775 ± 10 K for 30 min. The local grain boundary character was determined using precession enhanced automated crystallographic orientation maps and were collected with a 3 nm step size in a JEOL 2100 TEM [48]. Similarly, the elemental segregation behavior was collected using four energy disperse X-ray spectroscopy (EDS) detectors in a probe corrected FEI Titan [49] and analyzed for grain boundaries that were edge-on to the incident electron beam using the Cliff–Lorimer k-factor methodology [50].

Results

Upon constructing a bicrystal to determine the propensity for solute segregation, modelers typically assume that the global solute concentration, as would be measured experimentally, is present in the grains surrounding a given grain boundary. In a real microstructure, where many boundaries with potentially large differences in tendency to segregate solute exist, there will be competition for the same finite supply of solute. This means that boundaries will not all be surrounded by grain interiors with the global concentration. Thus, representing individual grain

boundaries as bicrystal systems with the global solute concentration is not realistic.

Once it is acknowledged that a better estimate of the local solute concentration is needed we ask: what constitutes a representative solute concentration at a grain boundary? To account for the presence of multiple boundaries with varying tendencies to segregate solute, a nanocrystalline Pt microstructure with nominal grain diameter of 5 nm is generated as previously described. After equilibration to 775 K, approach (a) is employed to determine the equilibrium distribution of Au solute with a global concentration of 5, 10, and 15$\%_{at}$Au. To obtain a realistic representative solute concentration at a grain boundary for use in MD models of individual GBs, the microstructure illustrated in Fig. 1 is examined to obtain the average amount of solute in the bulk crystalline (gray colored) region for a variety of global Au compositions. The concentration of solute in the bulk is calculated by determining the number of Au that are characterized by common neighbor analysis (CNA) [51, 52] as having a local face centered cubic (FCC) neighborhood, meaning that they are in the Pt grains. It is found that at 775 K only a few atomic layers near the grain boundary are not considered FCC, meaning that there are few defects that could change the number of Au considered to be in the bulk. A representative bulk concentration is calculated for various experimentally relevant global solute concentrations: a value of 15$\%_{at}$Au yielded 0.9$\%_{at}$Au, 10$\%_{at}$Au yielded 0.6$\%_{at}$Au, and 5$\%_{at}$Au yielded 0.36$\%_{at}$Au in the bulk Pt grains. Note that the bulk composition for a given overall composition will depend on the grain size with larger grains yielding larger bulk compositions. To relate the concentration in the bulk of the grains to a chemical potential for use in the semi-grand canonical MC model of approach (b), a series of Au chemical potentials were applied to bulk crystalline Pt to determine the relationship to bulk Au concentrations up to the solubility limit (see "Appendix 2" section). In this way, the segregation to the grain boundaries can be represented as a function of equivalent bulk concentration in the surrounding grains.

The concentration of Au in the bulk region of the grains contained in the microstructure of Fig. 1 is reasonable as the values are below the solubility limit according to the bulk phase diagram arising from the potential (see Fig. 11). The solubility limit is approximately 1$\%_{at}$Au at 775 K. Knowing a representative value for solute concentration in the bulk region of the grains, a more detailed examination is conducted for a number of planar bicrystal grain boundaries to generate representative levels of segregation. Employing approach (b) to populate the boundaries specified in Table 1, it is noted that the boundaries exhibit a sudden increase in excess Au with increasing chemical potential. This occurred for each of the boundaries in Table 1, but at varying critical chemical potentials (bulk concentrations) of Au as illustrated in Fig. 2. In addition, it is found that running the semi-grand canonical MC model of method (b) with the same chemical potential, but different random number seeds, can result in the Au excess converging to an alternate value. While ideally there would be a unique value of the excess for any chemical potential, the finite sampling of the MC simulations may not reach the true equilibrium configuration due to the need to nucleate and grow the other phase. This hysteresis-like behavior is indicative of a first-order phase transition. The phase transition occurs at bulk concentrations well below the bulk solubility limit of Au in Pt at 775 K. This fact demonstrates that the clustering of Au is not due to the nucleation of a bulk second phase particle, but rather to the effect of the grain boundary. The stochastic nature of the transition reflects the hysteresis associated with forming the high interfacial excess using method (b). To be assured that a separate phase is indeed formed at the boundary, the chemical potential of the Au at the grain boundary must be equal to that in the bulk.

To be sure that phase change behavior is not an artifact of the simulation conditions and ensure that the chemical potential of Au in the bulk is equal to that at the grain boundary, approach (a) is employed in an attempt to verify the conclusion that there is a

Table 1 The orientation of the crystal is specified by listing the planes forming the boundary of left and right crystal

CSL	PubID	Zone-axis	Planes
Σ5	n/a	⟨0 2 0⟩	(0 2 1 4)/(2 0 2)
Σ21	208	⟨5 3 1⟩	(8 5 1)/(3 1 0)
Σ55	219	⟨9 5 2⟩	(1 2 3 1)/(1 2 3 1)
Σ7	220	⟨1 5 3⟩	(1 2 3 1)/(9 8 3)

The publication identification number (PubID) refers to that used in the supplemental material of Ref. [24]. The Σ5 boundary is that defined in Ref. [54]. Plane indices are given in units of half of the lattice constant

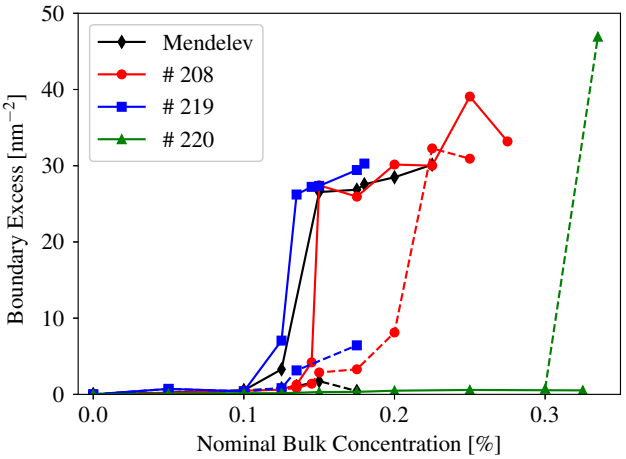

Figure 2 The semi-grand canonical ensemble hybrid MC/MD of approach (b) is used to calculate the excess Au concentration at the boundary is plotted versus the equivalent bulk concentration as defined by the chemical potential. All data was generated at a temperature of 775 K. Broken lines indicate the composition in the low-Au state and solid lines indicate that composition in the high-Au state. The boundaries are identified by their PubID listed in Table 1.

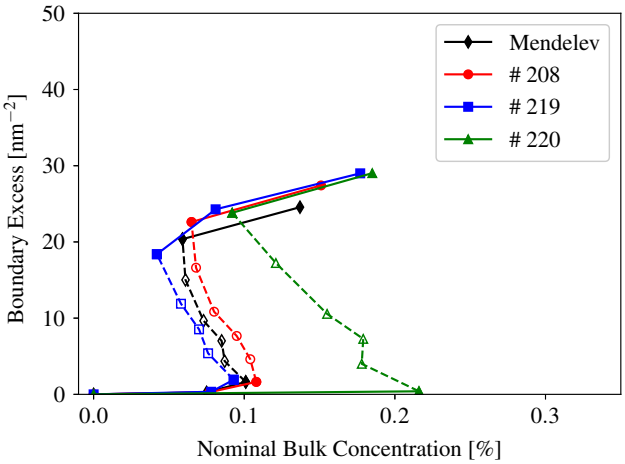

Figure 3 Canonical ensemble hybrid MC/MD calculation of the excess Au concentration at the boundary is plotted against the bulk concentration using approach (**a**). The lines connect simulaton points in order of increasing global Au concentration. The metastable compositions are linked by a dashed-line and marked by open symbols. All data was generated at a temperature of 775 K. The boundaries are identified by their PubID listed in Table 1.

first-order phase transition. In these simulations, Au atoms are initially placed at random in the bicrystal cell at varying overall concentrations. The hybrid MD/MC procedure is then employed to redistribute the fixed number of Au according to thermal equilibrium. After equilibration, the average bulk concentration and interfacial excess are computed. To obtain the bulk Au concentration, the average Au concentration in bulk-like regions on either side of the boundary is computed. The interfacial excess is obtained by determining the total Au content in the region of the boundary and subtracting the number of Au atoms expected based on the bulk concentration just determined. The plot of interfacial excess in Fig. 3 appears sigmoidal; characteristic of a first-order transition. The line connects simulated conditions in order of increasing global Au concentration and is meant as a guide to the eye to show the similarity with isotherms that exhibit a first-order phase transition where the thermodynamically metastable region is indicated by a dashed line. In the multi-valued regime, the interfacial excess corresponds to a thermodynamically metastable configuration which is stabilized in the current simulations by the fixed overall Au concentration. The possibility of this multi-valued behavior has been recently predicted in a diffuse interface model of interfacial segregation [34]. As with the results generated using approach (b), one sees that the bulk concentration at which the high interfacial excess occurs depends on the specific boundary and that the order of this dependence appears to be the same. Boundary 219 transitions at the lowest bulk concentration and boundary 220 transitions at the highest using either approach.

The nature of the the phase change at the grain boundaries is illustrated by the $\Sigma 5$ (Mendelev reference) boundary and boundary 208 in Figs. 4 and 5, respectively. In each case the Au is seen to be present both in the bulk and segregated to the grain boundary as expected. The nominal bulk concentration of $0.15\%_{at}$Au, as determined by the chemical potential, is identical in each case. In the low concentration phase (Figs. 4a, 5a) Au is observed to form Au-rich clusters on the grain boundary. In the high concentration phase (Figs. 4b, 5b) Au is supersaturated at the grain boundary according to the bulk solubility limit. This is not surprising due to Au being immiscible in Pt above about $1\%_{at}$Au at this temperature. However, the grain boundary phase appears to have a much lower solubility limit than bulk Pt in order to favor segregation well below the bulk solubility limit.

The formation of the Au-rich phase at the boundary may also result in defaceting of a grain boundary.

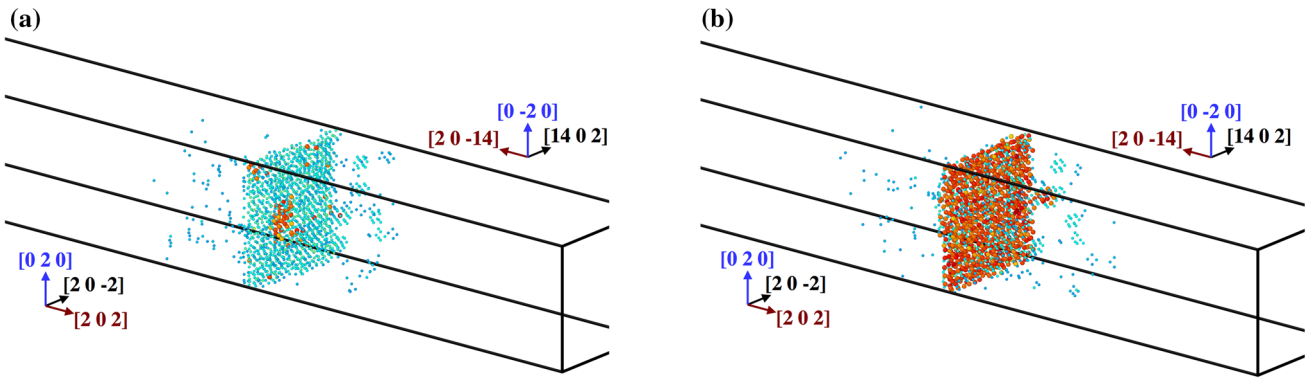

Figure 4 Illustration of the GB at **a** low, **b** high Au concentration segregation states for the Σ5 boundary. The color scheme is that used in Fig. 1 with FCC Pt atoms deleted for clarity. The location of Au was emphasized by decreasing the size of spheres representing Pt atoms. These figures were generated using approach (**b**). **a** Low segregation state, **b** High segregation state.

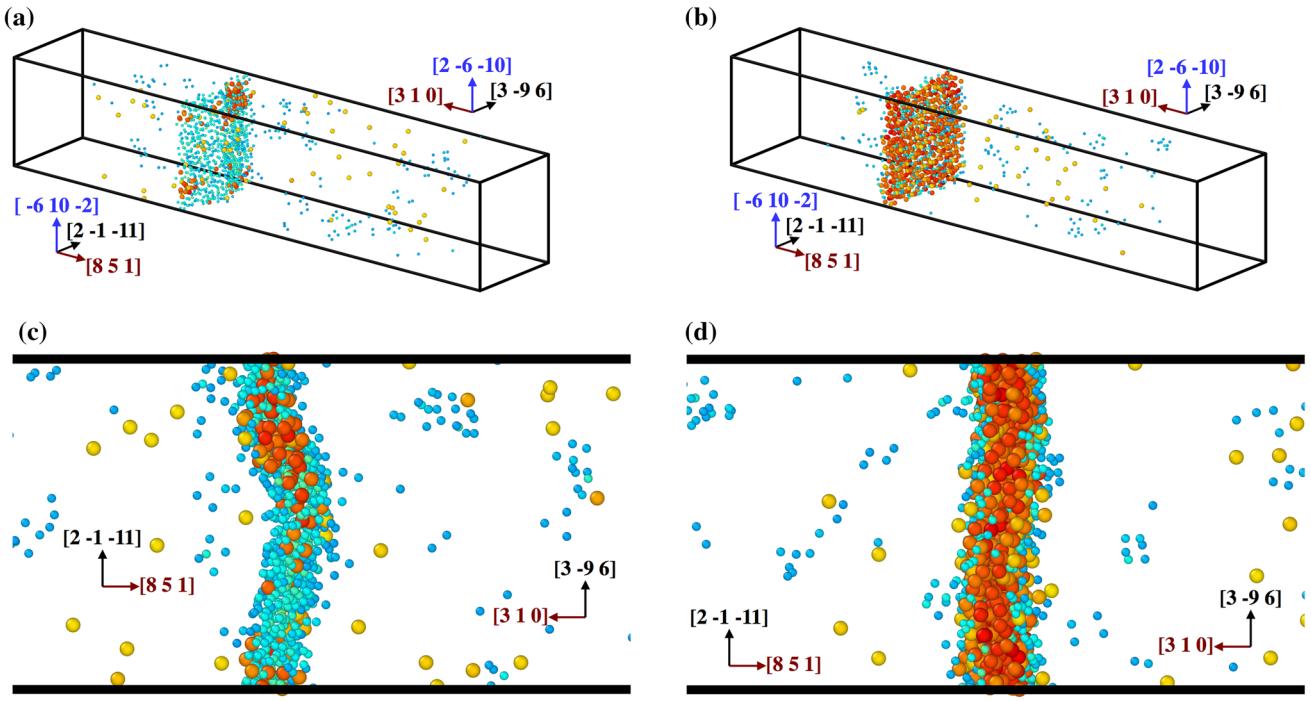

Figure 5 Illustration of the GB at **a** low, **b** high Au concentration segregation states for the boundary 208 as determined by approach (**b**). The color scheme is that used in Fig. 1 with FCC Pt atoms deleted for clarity and remaining Pt decreased in size relative to Au. A different projection of the grain boundary structure shows a defaceting transition occurring between the **c** low concentration state, **d** high concentration state. **a** Perspective view of low segregation state, **b** Persepctive view of high segregation state, **c** projection of low segregation state, **d** projection of high segregation state.

In the case of the boundary 208, the minimum energy structure of the boundary is planar, but at higher temperatures, the boundary spontaneously facets. The faceting illustrated in Fig. 5c is retained in the low Au segregation phase and is effectively eliminated in the high Au concentration phase illustrated in Fig. 5d.

The segregation behavior generated by approach (a) in the two-phase coexistence region is shown in Fig. 6. For all four of the boundaries shown, there is a clear separation within the boundary into dilute and highly concentrated Au. These regions correspond to the dilute and concentrated states of the boundary found in the semi-grand canonical MC/MD simulations generated by approach (b). The figures shown

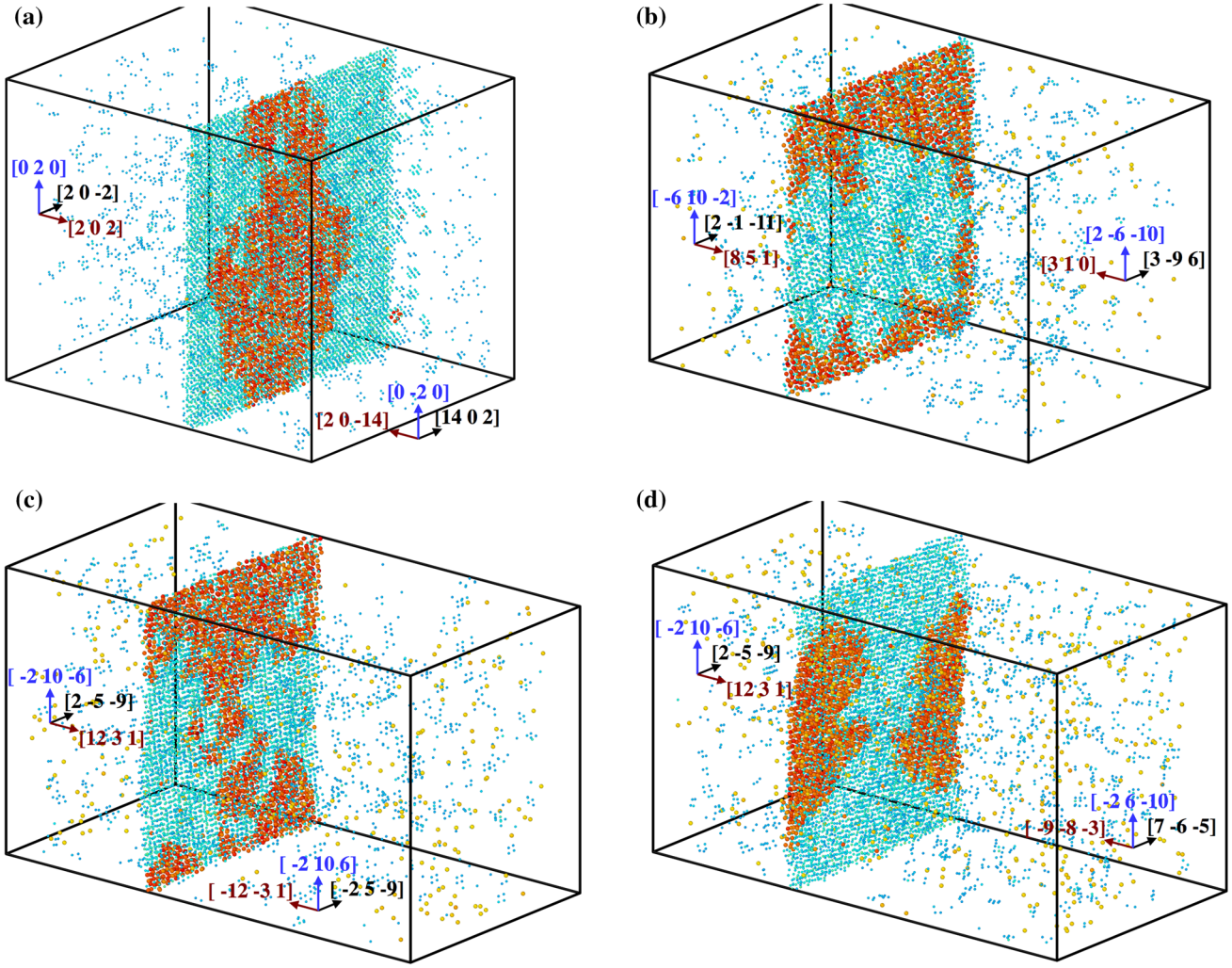

Figure 6 Illustration of the grain boundaries obtained in the canonical ensemble simulations (approach **a**) constrained to the two-phase region at a temperature of 775 K. The color scheme is that used in Fig. 1 with FCC Pt atoms deleted for clarity and the remaining Pt decreased in size relative to Au. **a** Mendelev Σ5 boundary, **b** #208, **c** #219, **d** #220.

are snapshots of the various boundaries. Note that the qualitative behavior of separation into two-phases is seen in all such snapshots, the regions of dilute and high Au concentration vary between snapshots indicating that the simulations are not frozen into a unique configuration.

Discussion and conclusions

The possibility of grain boundary phase transformations was proposed by [55] and has been considered by multiple authors over the years as discussed above. This work presents an explicit computational demonstration of such a grain boundary phase transformation for grain boundaries in the Pt–Au alloy system. In particular, this work demonstrates a phase transition between low and high levels of solute (Au) segregation to the boundary. We have examined in detail the segregation to four specific grain boundaries. The existence of the phase transformation for all of these boundaries suggests that this is the general behavior in this alloy system. This is not a surprising result. The bulk alloy thermodynamics of Pt–Au also shows a miscibility gap over most of the temperature range indicating an energetic preference for same-species neighbors. It is reasonable that this tendency would persist at grain

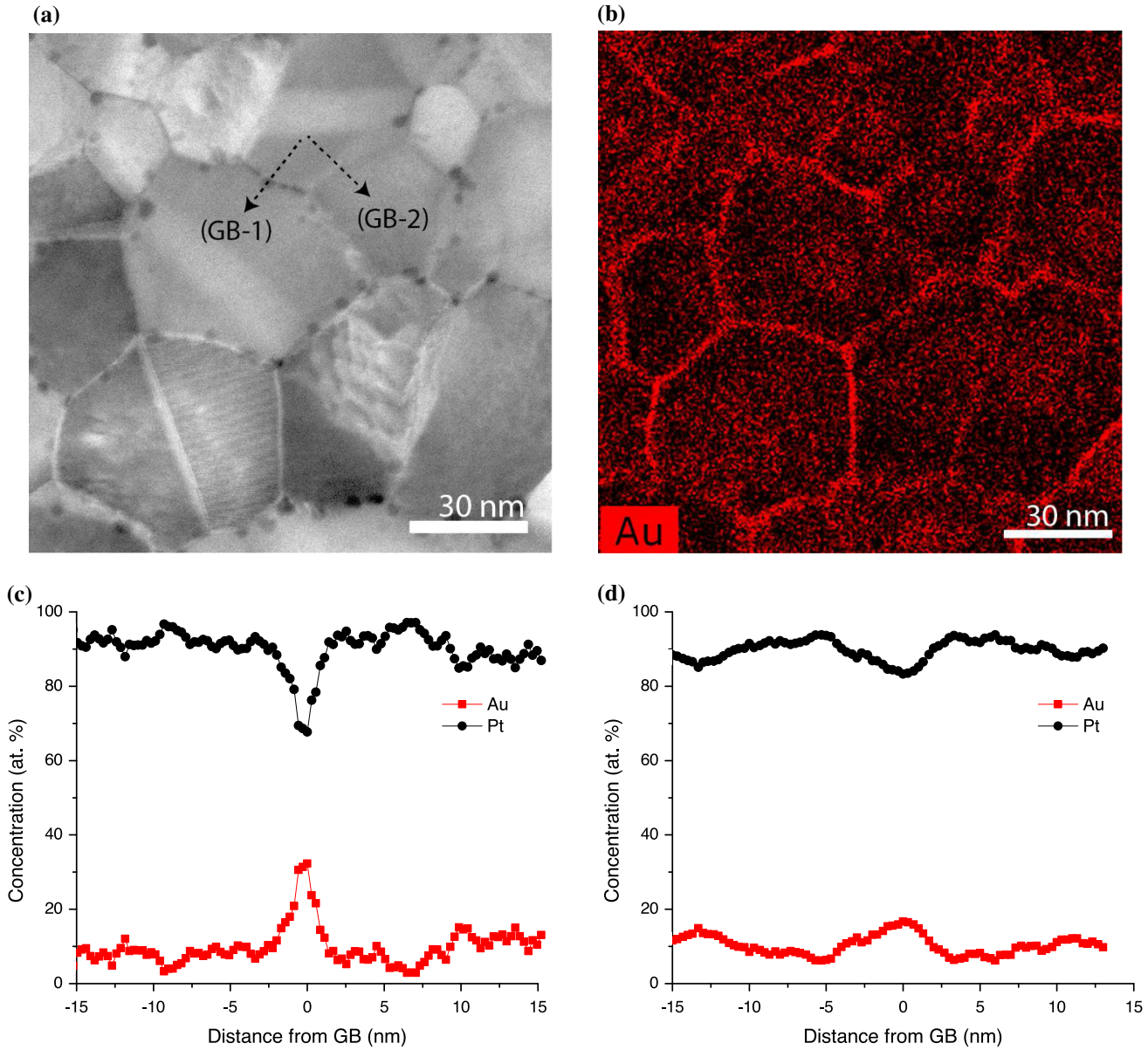

Figure 7 Experimental results were obtained by annealing a Pt-10$\%_{at}$Au film for 30 min at 775 K. **a** contains a HAADF image of the representative microstructure, **b** a STEM-EDS Au intensity map corresponding to the same area as shown in **a**. Comparing the two images indicates clear Au segregation anisotropy at grain boundaries. Dark circular regions located along some of the grain boundaries are voids. **a** HAADF image, **b** STEM-EDS Au intensity map, **c** GB-1: 50.8°⟨4 16 21⟩, **d** GB-2: 13.0°⟨4 8 1⟩.

boundaries and so lead to the two phase behavior. The other qualitative observation is that while all of the boundaries studied exhibit the two phase behavior, the bulk concentration (chemical potential) at which the transition occurs varies somewhat between boundaries.

The examination of the individual boundaries was motivated by the observation in Fig. 1 of significant inhomogeneity in the degree of segregation to grain boundaries in a nanocrystalline polycrystal. While one would expect different boundaries in a polycrystal to have somewhat different segregation tendencies, this result was surprising in that different boundaries appeared to either be only slightly segregated or very strongly segregated. This level of difference between boundaries is not consistent with a reasonable variation in heats of segregation between boundaries. Furthermore, large differences

in segregation were also found in the experimental microstructure of Fig. 7. The resolution of this is clear given the above observation of phase transformations in the boundaries. In the polycrystal, the bulk concentration is such that some of the boundaries equilibrate in their low segregation phase while others equilibrate in their high segregation phase consistent with the strong variation between the different boundaries in the polycrystal.

The results of MC models and experimental evidence from Pt-10$\%_{at}$Au films demonstrate that the segregation to nanocrystal grain boundaries is highly heterogeneous and is a potentially relevant factor in modeling the influence of segregation on nanocrystalline stability. Models of nanocrystalline stability typically simplify the theoretical treatment by treating all grain boundaries equivalently [2, 12, 14, 15]. This is a very reasonable first approximation, but the current results indicate that it can be a coarse simplification of the actual behavior. It should be noted that the current results are not inconsistent with the possible high stability of such alloy systems. As shown by [56], the pinning of a fraction of the grain boundaries can stop grain growth of the entire grain boundary network. In this case, it is reasonable to assume that the highly segregated boundaries may be pinned.

Qualitative validation of the MD simulation can be seen in Fig. 7 that shows experimental evidence of Au segregation in the Pt-10$\%_{at}$Au system even after a brief anneal for 30 min at 775 K (approximately 0.4 of the alloy's solidus temperature). Figure 7a, b correspond to a high angular annular dark field (HAADF) image and EDS map of the same spatial location, respectively. Though not a fully equilibrated microstructure, there is notable segregation anisotropy in a number of grain boundaries in Fig. 7b. Evidence for the sample not being fully equilibrated is in the composition of Au in the bulk-like region of the Pt grains. At the quoted annealing temperature, there should be less than 1$\%_{at}$Au in the grains according to the bulk alloy phase diagram. Two specific edge-on grain boundaries, which were fully characterized by precession enhanced automated crystallographic orientation and EDS maps, are shown in Fig. 7c, d. The distinctly different segregation line profiles which correspond to a random high angle grain boundary (misoriented 50.8° about the ⟨4 16 21⟩ zone axis) and low angle grain boundary (misoriented 13.0° about the ⟨4 8 1⟩ zone axis) validates the highly anisotropic nature of Au segregation as a function of grain boundary character found in the MD model.

This work points to multiple future lines of research. The results presented here are for a single temperature and so an exploration of the temperature dependence of these grain boundary phase transitions would be of interest. The current results only point to the equilibrium solute distribution and do not fully explore the kinetics of grain evolution in the presence of this heterogeneous alloy segregation. To this end, studies of the influence on both low and high levels of solute on boundary mobility and possible pinning are needed. Finally, the preliminary evidence for a segregation-induced defaceting transition in boundary 208 (Fig. 5c, d) is observed. However, it is not clear if the boundary spontaneously defaceted or if it was driven to do so by the solute. The possibility of solute induced defaceting was previously observed in grand canonical MC/MD models of inclined twin boundaries in the case of H in Ni [57]. The influence of solute segregation on faceting transitions is another important direction for future research.

Acknowledgements

The authors would like to thank Ping Lu of Sandia National Laboratories for sharing his expertise with imaging grain boundary segregation in this material system. The work was supported by the US Department of Energy, Office of Science, Materials Sciences and Engineering Division, under FWP Award #15013170. Sandia National Laboratories is a multimission laboratory managed and operated by National Technology and Engineering Solutions of Sandia LLC, a wholly owned subsidiary of Honeywell International Inc. for the US Department of Energy's National Nuclear Security Administration Under Contract DE-NA0003525.

Appendix 1: Pt–Au potential development

Calculation of reference structures

Due to the lack of measured properties for the PtAu alloy, we instead rely on density functional theory to provide forces and energies for ordered and disordered configurations with which the potentials will be parameterized; This strategy is referred to as force

matching [40]. In force matching, two databases are generated, one for parameterization and one for validation. The databases consist of a wide variety of configurations that represent a range of conditions at which the potential might be applied. Using the force-matching approach, individual properties are not reproduced, but rather the goal is to fit the interatomic forces and energies of a wide variety of systems. Since the fit must be applicable to grain boundaries that contain disordered regions at the boundary, it is necessary to fit the potentials for disordered solids in addition to crystalline phases. The actual structures do not need to be equilibrium ones, or even thermodynamically stable states as the DFT calculations only provide energies and forces with which to fit the potential.

Single element potentials are fit to a small range of lattice constants about equilibrium for the FCC, BCC, HCP, diamond, and disordered FCC structures. The disordered FCC structures included random displacements up to 0.1 Å. Also included in the database are multiple sample configurations of a liquid state at 2000 K. The fitting database for the alloy potential consists of a variety of structures including configurations of the liquid PtAu alloy at 2000 K, an FCC PtAu alloy with random displacements of up to 0.1 Å, a range of lattice constants for the ordered compounds $L_1 2$, B_1, and $L_2 0$.

Functional form of the potential

The cutoff function Ξ is applied to both the density and pair potential and takes the form

$$\Xi(\chi) = -6\chi^5 + 15\chi^4 - 10\chi^3 + 1 \qquad \text{where} \qquad \chi(r, r_c) = \frac{r - r_c}{r_{\text{cut}} - r_c} H(r_c). \tag{2}$$

The function H is the Heaviside step function switching at the inner cutoff r_c, and the global cutoff for the potential is r_{cut}. The pair and density functions each have their own inner cutoff radius defined as r_p and r_d, respectively.

The functional form of the pair potential employed is that of Morse [58],

$$\phi(r) = D_e \left\{ \left[1 - e^{-a_m (r - r_0)} \right]^2 - 1 \right\} \cdot \Xi(r, r_p), \tag{3}$$

where D_e and a_m are fitting parameters, and r_0 is the equilibrium bond distance as determined from DFT calculations. The electron density function is a simple exponential,

$$\rho(r) = \rho_0 e^{-\frac{r - r_0}{\lambda_0}} \cdot \Xi(r, r_d), \tag{4}$$

where ρ_0 and λ_0 are fitting parameters.

The embedding function is derived as done by Foiles [38] starting with the expression for the total energy of the EAM potential

$$E_{\text{tot}} = \sum_i F_i(\rho_i) + \frac{1}{2} \sum_{i,j} \phi_{ij}(r_{ij}) \qquad \text{where} \qquad \rho_i = \sum_{j \neq i} \rho(r_{ij}). \tag{5}$$

Foiles replaced the total energy function E_{tot} with the function from the Rose equation of state for metals [59] and solved Eq. 5 for the embedding functional. The Rose equation of state takes the form

$$E_{\text{Rose}}(r) = E_0 (1 + a^*) e^{-a^*}, \tag{6}$$

where E_0 is the cohesive energy and

$$a^* \equiv \frac{a - a_0}{a_0 \lambda_{\text{R}}}. \tag{7}$$

The a_0 term is the DFT calculated lattice constant and $\lambda_{\text{R}} = \sqrt{E_0/(9\Omega B)}$. This term contains the cohesive energy (E_0), bulk modulus (B), and atomic volume (Ω), which are obtained from experiments or, in this case, first-principles calculations. With the Rose equation of state incorporated into the potential, the λ_{R} term is guaranteed to be reproduced by the fit.

Procedure for fitting the potential

The actual fitting of the nine parameters was carried out using the Dakota [60] software package developed at Sandia National Laboratories. The optimization utilized the gradient and hessian free Collony pattern search algorithm. After each optimization step, Dakota called LAMMPS [44] that was used to determine the error between the energies and forces calculated with the EAM potential to the reference data. DAKOTA optimized the parameters until the change in the error (root of the sum of squares of the differences) was less than 1×10^{-3}.

The Rose equation of state is used to constrain the energy versus lattice constant relationship, the λ_{R} term is fixed using the DFT calculated values for each element. Consequently, there is some deviation in the

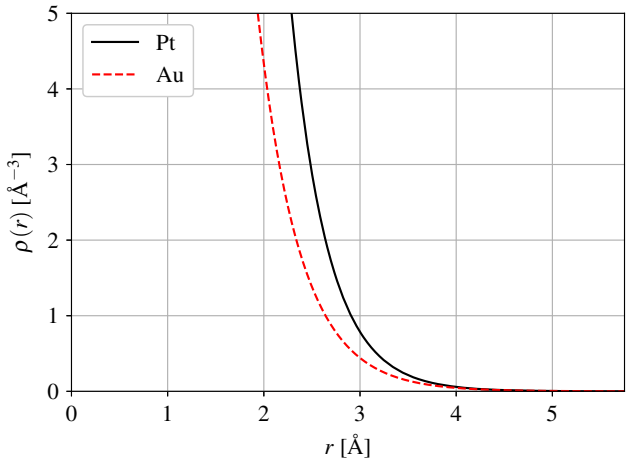

Figure 8 Electron densities for single element potentials.

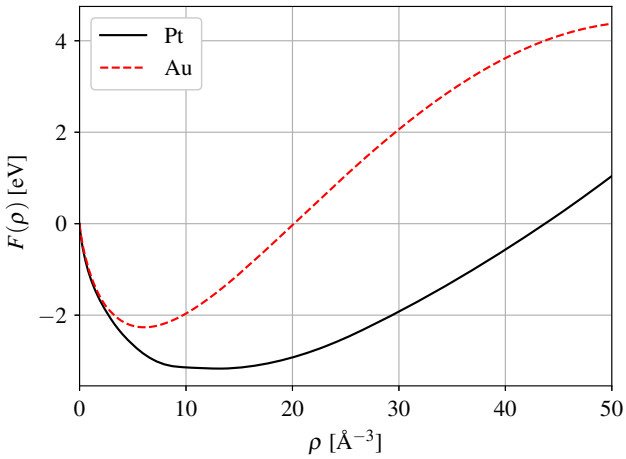

Figure 10 Embedding energies for single element potentials.

parameters for binding energy E_0, lattice constant a_0, and bulk modulus B, due to the λ_R quantity being constrained, rather than the constituent properties being restricted individually.

The maximum electron density is 50 Å^{-3}, and the cutoff for the potentials are 5.50 Å for Pt, and 5.75 Å for Au and PtAu. Since the cutoff parameter must be fixed initially in this scheme, a range of values were used and fits were attempted for each.

Results and validation of fits

Plots of the electron densities, embedding functional, and pair potentials obtained by the fitting procedure are provided in Figs. 8, 9 and 10. Validation of the elemental potentials is carried out for a number of cases, many are found in Table 2, in addition to comparisons to independent data of the elemental liquid at 2000 K and the FCC structure with random displacements. Specific geometries of interest are also included such as the intrinsic stacking fault, the $\Sigma3(111)\langle110\rangle$ (coherent twin) boundary, self-interstitial, vacancy, and the (111), (100), and (110) surfaces.

The force matching approach relies on the accuracy of the first principles calculations used to obtain forces and energies. However, there are inherent weaknesses in the GGA approach that result in deviation from experiment. For instance, GGA is known to calculate smaller cohesive energies than measured, and larger lattice constants. It is well known that the vacancy formation energy is poorly matched by GGA [61]. Consequently, the vacancy configuration was excluded from the fitting database, but is included in the validation database. Interestingly, the value of the vacancy formation energies calculated by the potential, reported in Table 2, are in general agreement with experimental values.

The validation database for the alloy potential includes independent data for the PtAu liquid and random PtAu FCC alloy. The overall error of the alloy fit to the parameterization database for energies and forces are 2.1796×10^{-2} and 5.3216×10^{-1}, respectively; Compare these error values to those obtained from applying the potential to the validation database of 9.2593×10^{-3} and 7.0764×10^{-1}. After validation of the binary fit, a number of tests were conducted to study the range of applicability of the potential for a number of relevant cases designed to represent grain boundary and surface segregation. The results of these tests are reported in Table 3. Although the absolute errors are rather large for segregation, it was deemed to be acceptable as the

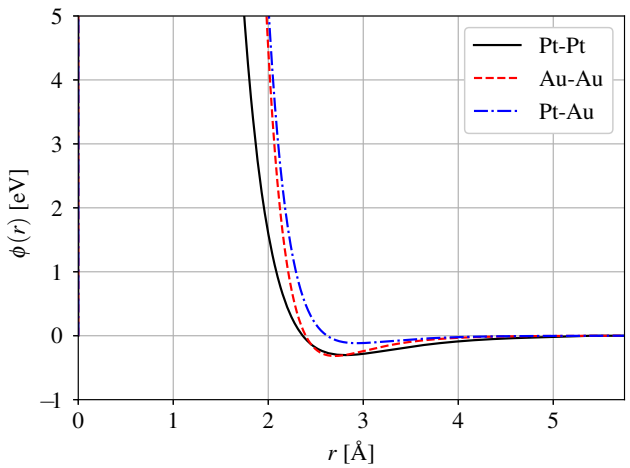

Figure 9 Pair potentials.

Table 2 Sample values resulting from the fit of single element potentials

Property	Pt			Au		
	DFT	MD	Ref	DFT	MD	Ref
Fit						
E_0	− 5.5057	− 5.5050	− 5.77[b]	− 3.0374	− 3.0374	− 3.93[b]
a_0	3.9764	3.9757	3.92[a]	4.1537	4.1537	4.08[a]
B	235.9186	236.0700	283[c]	146.1305	146.0097	167[c]
E Error	–	1.8124×10^{-2}	–	–	8.0244×10^{-3}	–
F Error	–	5.7046×10^{-1}	–	–	2.8579×10^{-1}	–
Validation						
$E_{BCC} - E_{FCC}$	0.0764	0.0571	–	0.0085	0.0366	–
ISF	307.2131	168.0494	332[d]	43.6539	67.8987	45[d], 50[f]
Twin	117.6568	33.4571	161[d]	10.2408	55.2048	23[d]
Vac	0.6848	1.9773	1.51[e]	0.4708	1.2225	0.95[e]
Int	5.3159	4.2845	–	3.0537	3.7485	–
$\gamma(100)$	1833.6088	1742.8123	2480[g]	954.3534	667.0252	1710[g]
$\gamma(110)$	1884.3808	1884.3808	–	922.0133	723.9978	1790[g]
$\gamma(111)$	1464.8728	1649.2121	2350[g]	707.9624	617.3931	1610[g]
C_{11}	279.2820	264.3480	347[c]	146.4985	168.4316	186[c]
C_{12}	214.2369	221.9309	251[c]	145.9465	134.7988	157[c]
C_{44}	65.8006	68.7821	76.5[c]	25.5122	44.2999	42[c]
E error	–	1.8809×10^{-2}	–	–	1.0272×10^{-2}	–
F error	–	4.1539×10^{-1}	–	–	3.1137×10^{-1}	–

The parameters are: E_0 binding energy, a_0 lattice constant, B bulk modulus, *ISF* intrinsic stacking fault energy, *Twin* $\Sigma 3(111)\langle 1\bar{1}0\rangle$ grain boundary energy, *Vac* relaxed vacancy energy in FCC lattice, *Int* relaxed self interstitial energy in FCC lattice, C_{xx} compliance coefficients, B bulk modulus (calculated with $\frac{1}{3}(C_{11} + 2C_{12})$). Energies are given in eV, surface energies in $\mathrm{mJ} \cdot \mathrm{m}^{-2}$, lattice constants in Å, and pressures in MPa

[a]Ref. [62]

[b]Ref. [63]

[c]Ref. [64]

[d]Ref. [65]

[e]Ref. [66]

[f]Ref. [67] and references therein

[g]Ref. [68]

sign of the segregation energy and the relative magnitudes are similar. The largest errors present in the table occur for the test of site segregation energies to the Σ5 grain boundary. The large errors in the smallest segregation energies is to be expected as the small energy change makes it more difficult to obtain an accurate measure of the small change in system energy. The preference for surface segregation of Au on to Pt surfaces predicted by the potential is Reassuringly, the bulk site-substitution energies are in excellent agreement. A further test of the behavior of the potential was made by constructing a phase diagram for the alloy as illustrated in Fig. 11. The solubility values are in very good agreement with experimental phase diagrams reported in the literature.

Table 3 Testing of PtAu potential in situations relevant to the current study

	DFT	MD	Error (%)
Σ5 site substitution			
Site 1	0.1214	− 0.1982	− 263.168
Site 2	− 1.2127	− 0.7805	− 35.637
Site 3	− 0.0744	− 0.1982	166.257
Site 4	− 1.2138	− 0.7805	− 35.696
(1 1 1) Surface site substitution			
Pt(111)-surf	− 0.4051	− 0.1061	89.210
Pt(111)-subsurf	− 0.7665	0.0121	− 111.389
Bulk site substitution			
Au in Pt(111)	2.75394	2.810275	2.046

The Σ5 substitution test compares the energy differences for DFT and MD calculations for the energy difference (in eV) between a reference site away from the Σ5(310) tilt grain boundary and an atom in one of four non-equivalent positions at the boundary. The surface site substitution test examines the difference in energy for the substitution of layers of Pd atoms at different depths in (111) Pt surface slabs. Errors are reported in percent difference from the value calculated with DFT.

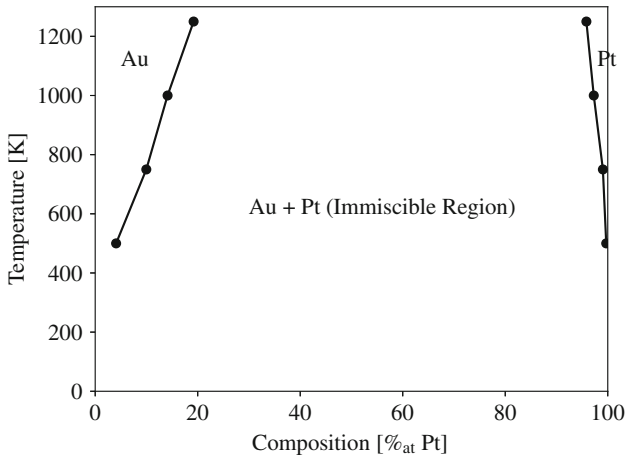

Figure 11 Partial phase diagram of the PtAu system as calculated via the potential developed for this work.

Coefficients of fits to analytical functions

The coefficients of the parameters in Eqs. 2–4 need to generate the elemental potentials are found in Table 4, and the parameters need for the Pt–Au pair potential are found in Table 5.

Table 4 Coefficients for the fitting of single element potentials

Coefficient	Pt	Au
E_0	− 5.5056688400	− 3.0330710327
r_0	2.8117394047	2.9371094370
a_m	1.5466362282	2.1869362276
λ_R	0.1625746000	0.1437112170
ρ_0	1.2851435943	1.3619497798
λ_0	0.3845403249	0.4378868737
D_e	0.3023110161	0.1162978385
r_p	5.0023688660	5.7305726517
r_d	5.0082001634	5.6306726014

The parameters are used in Eqs. 2, 3, and 4

Table 5 Coefficients for the fit of Eq. 3 for the binary alloy potential

Coefficient	PtAu
r_0	2.7005171343
ρ_0	0.5099937463
a_m	2.2672956035
D_e	0.3166643333
r_p	5.2909653593

Appendix 2: Polynomial fits to properties of the PtAu potential

The chemical potential difference $\Delta\mu$ at 775 K between Pt and Au is expressed in terms of the absolute atomic concentration c of Au in Pt at 775 K is given in units of eV as

$$\Delta\mu(775\,\mathrm{K}) = \ln\left(\frac{c}{3.570602 \times 10^{-19}}\right) / - 15.13308, \quad (8)$$

where $c \leq 0.01$, the solubility limit.

Polynomial fit of the lattice constant $a(T)$ with respect to temperature is reported in Table 6 using the fitting function:

$$f(T) = AT^3 + BT^2 + CT + D. \quad (9)$$

Table 6 Polynomial fit to the lattice constant $a(T)$ with respect to temperature according to the form of Eq. 9

Element	Property (Å)	A	B	C	D
Pt	$a(0\,\mathrm{K} \le T \le 2000\,\mathrm{K})$	9.0281×10^{-12}	-1.5472×10^{-8}	2.8564×10^{-5}	3.9757
Au	$a(0\,\mathrm{K} \le T \le 1200\,\mathrm{K})$	3.6985×10^{-12}	2.1535×10^{-8}	7.3391×10^{-5}	4.1537

Electronic supplementary material: The online version of this article (doi:10.1007/s10853-017-1706-1) contains supplementary material, which is available to authorized users.

References

[1] Gleiter H (1989) Nanocrystalline materials. Prog Mater Sci 33:223–315

[2] Chookajorn T, Schuh CA (2014) Nanoscale segregation behavior and high-temperature stability of nanocrystalline W-20at.% Ti. Acta Mater 73:128–138. doi:10.1016/j.actamat.2014.03.039

[3] Chookajorn T, Park M, Schuh CA (2015) Duplex nanocrystalline alloy: entropic nanostructure stabilization and a case study on W–Cr. J Mater Res 30:151–163. doi:10.1557/jmr.2014.385

[4] Hornbuckle BC, Rojhirunsakool T, Rajagopalan M, Alam T, Purja Pun GP, Banerjee R, Solanki KN, Mishin Y, Kecskes LJ, Darling KA (2015) Effect of Ta solute concentration on the microstructural evolution in immiscible Cu–Ta alloys. JOM 67(12):2802–2809. doi:10.1007/s11837-015-1643-x

[5] Kurz S, Leineweber A, Mittemeijer E (2014) Anomalously high density and thermal stability of nanotwins in Ni(W) thin films: quantitative analysis by X-ray diffraction. J Mater Res 29(15):1642–1655. doi:10.1557/jmr.2014.202

[6] Khalajhedayati A, Rupert TJ (2015) High-temperature stability and grain boundary complexion formation in a nanocrystalline Cu–Zr alloy. JOM 67(12):2788–2801. doi:10.1007/s11837-015-1644-9

[7] Darling K, VanLeeuwen B, Koch C, Scattergood R (2010) Thermal stability of nanocrystalline Fe–Zr alloys. Mater Sci Eng A 527(15):3572–3580. doi:10.1016/j.msea.2010.02.043

[8] Darling KA, Chan RN, Wong PZ, Semones JE, Scattergood RO, Koch CC (2008) Grain-size stabilization in nanocrystalline FeZr alloys. Scr Mater 59(5):530–533. doi:10.1016/j.scriptamat.2008.04.045

[9] Millett PC, Selvam RP, Saxena A (2006) Molecular dynamics simulations of grain size stabilization in nanocrystalline materials by addition of dopants. Acta Mater 54(2):297–303. doi:10.1016/j.actamat.2005.07.024

[10] Weissmüller J (1993) Alloy effects in nanostructures. Nanostruct Mater 3(2):261–272. doi:10.1016/0965-9773(93)90088-S

[11] Koch CC, Scattergood RO, Saber M, Kotan H (2013) High temperature stabilization of nanocrystalline grain size: thermodynamic versus kinetic strategies. J Mater Res 28(13):1785–1791. doi:10.1557/jmr.2012.429

[12] Kalidindi AR, Chookajorn T, Schuh CA (2015) Nanocrystalline materials at equilibrium: a thermodynamic review. JOM 67(12):2834–2843. doi:10.1007/s11837-015-1636-9

[13] Andrievski RA (2014) Review of thermal stability of nanomaterials. J Mater Sci 49(4):1449–1460. doi:10.1007/s10853-013-7836-1

[14] Trelewicz JR, Schuh CA (2009) Grain boundary segregation and thermodynamically stable binary nanocrystalline alloys. Phys Rev B 79(9):094112. doi:10.1103/PhysRevB.79.094112

[15] Murdoch HA, Schuh CA (2013) Estimation of grain boundary segregation enthalpy and its role in stable nanocrystalline alloy design. J Mater Res 28(16):2154–2163. doi:10.1557/jmr.2013.211

[16] Darling K, Tschopp M, VanLeeuwen B, Atwater M, Liu Z (2014) Mitigating grain growth in binary nanocrystalline alloys through solute selection based on thermodynamic stability maps. Comput Mater Sci 84:255–266. doi:10.1016/j.commatsci.2013.10.018

[17] Kalidindi AR, Schuh CA (2017) Phase transitions in stable nanocrystalline alloys. J Mater Res 32(11):1993–2002. doi:10.1557/jmr.2017.188

[18] Phillpot SR, Wolf D, Gleiter H (1995) A structural model for grain boundaries in nanocrystalline materials. Scr Metall Mater 33(8):1245–1251. doi:10.1016/0956-716X(95)00350-5

[19] Cantwell PR, Tang M, Dillon SJ, Luo J, Rohrer GS, Harmer MP (2013) Grain boundary complexions. Acta Mater 62(152):1–48. doi:10.1016/j.actamat.2013.07.037

[20] Han J, Vitek V, Srolovitz DJ (2016) Grain-boundary metastability and its statistical properties. Acta Mater 104:259–273. doi:10.1016/j.actamat.2015.11.035

[21] Homer ER, Holm EA, Foiles SM, Olmsted DL (2014) Trends in grain boundary mobility: survey of motion mechanisms. JOM 66(1):114–120. doi:10.1007/s11837-013-0801-2

[22] Olmsted DL, Foiles SM, Holm EA (2009) Survey of computed grain boundary properties in face-centered cubic

metals: I. Grain boundary energy. Acta Mater 57(13):3694–3703. doi:10.1016/j.actamat.2009.04.007

[23] Ratanaphan S, Olmsted DL, Bulatov VV, Holm EA, Rollett AD, Rohrer GS (2015) Grain boundary energies in body-centered cubic metals. Acta Mater 88:346–354. doi:10.1016/j.actamat.2015.01.069

[24] Olmsted DL, Holm EA, Foiles SM (2009) Survey of computed grain boundary properties in face-centered cubic metals—II: grain boundary mobility. Acta Mater 57(13):3704–3713. doi:10.1016/j.actamat.2009.04.015

[25] Barr CM, Vetterick GA, Unocic KA, Hattar K, Bai XM, Taheri ML (2014) Anisotropic radiation-induced segregation in 316L austenitic stainless steel with grain boundary character. Acta Mater 67:145–155. doi:10.1016/j.actamat.2013.11.060

[26] Barr CM, Barnard L, Nathaniel JE, Hattar K, Unocic KA, Szlurfarska I, Morgan D, Taheri ML (2015) Grain boundary character dependence of radiation-induced segregation in a model Ni–Cr alloy. J Mater Res 30(09):1290–1299. doi:10.1557/jmr.2015.34

[27] Diercks DR, Tong J, Zhu H, Kee R, Baure G, Nino JC, O'Hayre R, Gorman BP (2016) Three-dimensional quantification of composition and electrostatic potential at individual grain boundaries in doped ceria. J Mater Chem A 4(14):5167–5175. doi:10.1039/C5TA10064J

[28] Herbig M, Raabe D, Li YJ, Choi P, Zaefferer S, Goto S (2014) Atomic-scale quantification of grain boundary segregation in nanocrystalline material. Phys Rev Lett 112(12):126103. doi:10.1103/PhysRevLett.112.126103

[29] Yao L, Ringer S, Cairney J, Miller M (2013) The anatomy of grain boundaries: their structure and atomic-level solute distribution. Scr Mater 69(8):622–625. doi:10.1016/j.scriptamat.2013.07.013

[30] Sickafus K, Sass S (1987) Grain boundary structural transformations induced by solute segregation. Acta Metall 35(1):69–79. doi:10.1016/0001-6160(87)90214-8

[31] Wynblatt P, Chatain D (2008) Solid-state wetting transitions at grain boundaries. Mater Sci Eng A 495(1–2):119–125. doi:10.1016/j.msea.2007.09.091

[32] Wynblatt P, Liu Y (1992) Two-dimensional phase transitions associated with surface miscibility gaps. J Vac Sci Technol A: Vac Surf Films 10(4):2709–2717. doi:10.1116/1.577963

[33] Cheng WC, Wynblatt P (1997) Equilibrium form of PbBiNi alloy crystals. J Cryst Growth 173(3–4):513–527. doi:10.1016/S0022-0248(96)01049-4

[34] Abdeljawad F, Lu P, Argibay N, Clark BG, Boyce BL, Foiles SM (2017) Grain boundary segregation in immiscible nanocrystalline alloys. Acta Mater 126:528–539. doi:10.1016/j.actamat.2016.12.036

[35] Bishop CM, Cannon RM, Carter WC (2005) A diffuse interface model of interfaces: grain boundaries in silicon nitride. Acta Mater 53(18):4755–4764. doi:10.1016/j.actamat.2005.07.008

[36] Tang M, Carter WC, Cannon RM (2006) Grain boundary transitions in binary alloys. Phys Rev Lett 97(7):075502. doi:10.1103/PhysRevLett.97.075502

[37] Clark BG, Hattar K, Marshall MT, Chookajorn T, Boyce BL, Schuh CA (2016) Thermal stability comparison of nanocrystalline Fe-based binary alloy pairs. JOM 68(6):1625–1633. doi:10.1007/s11837-016-1868-3

[38] Foiles S, Baskes M, Daw M (1986) Embedded-atom-method functions for the fcc metals Cu, Ag, Au, Ni, Pd, Pt, and their alloys. Phys Rev B 33(12):7983–7991. doi:10.1103/PhysRevB.33.7983

[39] Foiles S, Baskes M, Daw M (1988) Erratum: embedded-atom-method functions for the fcc metals Cu, Ag, Au, Ni, Pd, Pt, and their alloys. Phys Rev B 37(17):10378–10378. doi:10.1103/PhysRevB.37.10378

[40] Ercolessi F, Adams JB (1994) Interatomic potentials from first-principles calculations: the force-matching method. Europhys Lett 26(8):583. doi:10.1209/0295-5075/26/8/005 (9306054)

[41] Foiles SM (1985) Calculation of the surface segregation of Ni–Cu alloys with the use of the embedded-atom method. Phys Rev B 32(12):7685–7693. doi:10.1103/PhysRevB.32.7685

[42] Seki A, Seidman D, Oh Y, Foiles S (1991) Monte Carlo simulations of segregation at [001] twist boundaries in a Pt(Au) alloy—I. Results. Acta Metall Mater 39(12):3167–3177. doi:10.1016/0956-7151(91)90051-2

[43] Seki A, Seidman D, Oh Y, Foiles S (1991) Monte Carlo simulations of segregation at [001] twist boundaries in a Pt(Au) alloy—II. Discussion. Acta Metall Mater 39(12):3179–3185. doi:10.1016/0956-7151(91)90052-3

[44] Plimpton S (1995) Fast parallel algorithms for short-range molecular dynamics. J Comput Phys 117(1):1–19. doi:10.1006/jcph.1995.1039

[45] Sadigh B, Erhart P, Stukowski A, Caro A, Martinez E, Zepeda-Ruiz L (2012) Scalable parallel Monte Carlo algorithm for atomistic simulations of precipitation in alloys. Phys Rev B Condens Matter Mater Phys 85(18):184203. doi:10.1103/PhysRevB.85.184203 (1012.5082)

[46] Gruber J, Lim H, Abdeljawad F, Foiles S, Tucker GJ (2017) Development of physically based atomistic microstructures: the effect on the mechanical response of polycrystals. Comput Mater Sci 128:29–36. doi:10.1016/j.commatsci.2016.07.011

[47] Cahn JW (1977) Thermodynamics of solid and fluid surfaces. In: Johnson WC, Blakely JM (eds) Interfacial

segregation. American Society of Metals, Metals Park, pp 193–228

[48] Hattar K, Bufford D, Buller D (2014) Concurrent in situ ion irradiation transmission electron microscope. Nucl Instrum Methods Phys Res Sect B: Beam Interact Mater Atoms 338:56–65. doi:10.1016/j.nimb.2014.08.002

[49] Argibay N, Brumbach MT, Dugger MT, Kotula PG (2013) Grain boundary diffusivity of Ni in Au thin films and the associated degradation in electrical contact resistance due to surface oxide film formation. J Appl Phys 113(11):114906. doi:10.1063/1.4795768

[50] Williams DB, Carter CB (2009) Transmission electron microscopy, 2nd edn. Springer, Boston. doi:10.1007/978-0-387-76501-3

[51] Faken D, Jónsson H (1994) Systematic analysis of local atomic structure combined with 3D computer graphics. Comput Mater Sci 2(2):279–286. doi:10.1016/0927-0256(94)90109-0

[52] Tsuzuki H, Branicio PS, Rino JP (2007) Structural characterization of deformed crystals by analysis of common atomic neighborhood. Comput Phys Commun 177(6):518–523. doi:10.1016/j.cpc.2007.05.018

[53] Kelchner CL, Plimpton SJ, Hamilton JC (1998) Dislocation nucleation and defect structure during surface indentation. Phys Rev B 58(17):11085–11088. doi:10.1103/PhysRevB.58.11085

[54] Mendelev MI, Deng C, Schuh CA, Srolovitz DJ (2013) Comparison of molecular dynamics simulation methods for the study of grain boundary migration. Model Simul Mater Sci Eng 21(4):045017. doi:10.1088/0965-0393/21/4/045017

[55] Hart EW (1968) Two-dimensional phase transformation in grain boundaries. Scr Metall 2(3):179–182. doi:10.1016/0036-9748(68)90222-6

[56] Holm EA, Foiles SM (2010) How grain growth stops: a mechanism for grain-growth stagnation in pure materials. Science 328(5982):1138–1141. doi:10.1126/science.1187833

[57] O'Brien CJ, Foiles SM (2016) Hydrogen segregation to inclined twin grain boundaries in nickel. Philos Mag 96(26):2808–2828. doi:10.1080/14786435.2016.1217094

[58] Morse PM (1929) Diatomic molecules according to the wave mechanics. II. Vibrational levels. Phys Rev 34(1):57–64. doi:10.1103/PhysRev.34.57

[59] Rose JH, Smith JR, Guinea F, Ferrante J (1984) Universal features of the equation of state of metals. Phys Rev B 29(6):2963–2969. doi:10.1103/Physrevb.29.2963

[60] Adams BM, Dalbey KR, Eldred MS, Gay DM, Swiler LP, Bohnhoff WJ, Eddy JP, Haskell K (2014) DAKOTA, a multilevel parallel object-oriented framework for design optimization, parameter estimation, uncertainty quantification, and sensitivity analysis (SAND2014-4633)

[61] Mattsson T, Mattsson A (2002) Calculating the vacancy formation energy in metals: Pt, Pd, and Mo. Phys Rev B 66(21):214110. doi:10.1103/PhysRevB.66.214110

[62] Smith CJ (ed) (1976) Smithells metals reference book, 5th edn. Butterworths, London

[63] Ashcroft NW, Mermin ND (1976) Solid state physics. Holt, Rinehart and Winston, New York

[64] Simmons G, Wang H (1971) Single Crystal elastic constants and calculated aggregate properties: a handbook. MIT Press, Cambridge

[65] Murr L (1972) Temperature coefficient of twin-boundary energy: the determination of stacking-fault energy from the coherent twin-boundary energy in pure F.C.C. metals. Scr Metall 6(3):203–208. doi:10.1016/0036-9748(72)90168-8

[66] Balluffi R (1978) Vacancy defect mobilities and binding energies obtained from annealing studies. J Nucl Mater 69–70:240–263. doi:10.1016/0022-3115(78)90247-7

[67] Gallagher PCJ (1970) The influence of alloying, temperature, and related effects on the stacking fault energy. Metall Trans 1(9):2429–2461. doi:10.1007/BF03038370

[68] Skriver HL, Rosengaard NM (1992) Surface energy and work function of elemental metals. Phys Rev B 46(11):7157–7168. doi:10.1103/PhysRevB.46.7157